Eur. Phys. J. C (2025) 85:998
https://doi.org/10.1140/epjc/s10052-025-14740-7

THE EUROPEAN PHYSICAL JOURNAL C

Regular Article - Theoretical Physics

Wormholes construction through the diverse dark matter density profiles

Z. Yousaf[1,a], **M. Rizwan**[1,b], **Mohammad Alshammari**[2,c], **Othman Abdullah Almatroud**[2,d], **Saleh Alshammari**[2,e], **M. Mossa Al-sawalha**[2,f]

[1] Institute of Mathematics, University of the Punjab, Lahore 54590, Pakistan
[2] Department of Mathematics, College of Science, University of Ha'il, Ha'il 2440, Saudi Arabia

Received: 9 August 2025 / Accepted: 3 September 2025

Abstract In this manuscript, we study traversable wormhole configurations under the influence of different dark matter density models, including Burkert, Moore, and Einasto density profiles. By using these density distributions, we construct wormhole configurations and find out the unknowns involved in the field equations. Finding the importance of dark matter in the hunt for traversable wormhole solutions inside galactic halos is the main goal of the current work. In order to gain a deeper comprehension of the physical plausibility and structural stability of the wormhole configurations, we examine the behavior of essential physical quantities, including the breaching of the null energy conditions, active gravitational mass, the equation of state, and the conservation of the stress-energy tensor. Additionally, we study the behavior of the complexity factor associated with each density model. From the analysis of these physical quantities, we show that the resulting wormhole solutions from each density model deviates from the null energy conditions, indicating that the wormhole configurations are supported by dark matter in order to survive in the galactic halos and exhibit viability.

1 Introduction

Newton claimed that gravity is an attraction that exists in both absolute space and time. Einstein defined it as a spacetime curvature due to mass and energy, which contradicts Newton's theory. According to Einstein's relativistic ideas, space and time are a singular continuum. While General relativity (GR) proposed that heavy objects curve spacetime and affect the time flow and velocity of other objects, Special Relativity (SR) stipulated that distance and time are relative to the motion of an observer. This novel idea helped to provide a more precise and comprehensive explanation of the universe by describing phenomena like gravitational lensing and Mercury's orbital precession that Newton's theory was unable to account for [1]. At the beginning of the 20th century, Einstein challenged Newton's dissertation that time and length were absolute since they lacked a physical foundation. He maintained that this notion cannot be included in the understanding of the physical cosmos. Einstein's thinking was influenced by the Michelson-Morley experiment, which showed that the earth did not appear to be moving through the luminiferous ether. This prompted Einstein to form the SR, which also ended up removing inconsistencies in Maxwell's electromagnetism theory [1]. In Einstein's view, such theories were inconsistent with Galilean kinematics, namely the law of addition of velocity, where moving observers with respect to one another would not at all experience the velocity of a signal of light. To address this enigma, Einstein investigated the synchronization of distant clocks. Though he was motivated by the work of Michelson-Morley, he did not investigate the forces on objects moving through the aether in developing SR. There are two fundamental principles that are the foundation for this concept [2].

Within four years of Einstein developing SR, the understanding of algebraic ideas started to change rapidly. It was suggested by the famous physicist Minkowski that it was very beneficial to use just four coordinates (x_1, x_2, x_3, x_4) inside a 4D spacetime domain. This marked a revolutionary

[a] e-mail: zeeshan.math@pu.edu.pk (corresponding author)
[b] e-mail: mrizwan.math@gmail.com
[c] e-mail: dar.alshammari@uoh.edu.sa
[d] e-mail: o.almatroud@uoh.edu.sa
[e] e-mail: saleh.alshammari@uoh.edu.sa
[f] e-mail: m.alswalha@uoh.edu.sa

Published online: 16 September 2025

shift in theoretical philosophy that impacted GR in turn. A marvel of human ingenuity, GR supplants Newtonian theory of gravitation with a geometric model of spacetime that permits accelerating systems of reference [3]. The easiest to comprehend is Albert Einstein's GR. The Einstein field equations (EFE) provide the foundation of GR. These equations consist of ten interrelated nonlinear partial differential equations that combine elliptic and hyperbolic properties. Among the mathematical elements that are utilized to define them are the curvature invariants, the metric tensor and the Ricci tensor [4]. There is much interest in the search for an exotic object theory in GR as found in the literature. The EFE most probably has WHs as one of its solutions [5,6]. Connections between two branes, cosmology, or even just two points on the manifold are referred to as WHs. In 1935, Einstein and Rosen [7] discovered the Einstein Rosen bridge, one of the earliest WH solutions. The Einstein-Rosen WH was initially demonstrated to be non-traversable since anything, even not a photon, could traverse its throat because of its rapid expansion and contraction [8]. However, Morris and Thorne later overcame WH traversability [3]. The Schwarzschild WH [10,11] is a solution to one of the first WH solutions in the Schwarzschild metric of a forever existing black hole. However, it came out too suddenly. That is, WHs can be supported if there exists a special kind of matter (i.e., exotic matter) with negative energy density [12–16].

As WHs have never been observed, there is intense argument regarding their existence and how they form. Yet, the potential for possessing an extendable WH or fabricating one in a laboratory in the distant future justifies the work of theorists and has garnered much attention in recent times [17–20]. Gravitational repulsion is necessary for WHs that can be traversed. This repulsion is often supplied by matters that have negative kinetic terms, which prevents the throat from collapsing. The gravitational theory must be modified to provide examples of WHs without the addition of such phantom matter [21–27]. In such theories, WHs are often unstable to linear perturbations [28–30]. Because of vacuum polarization nearby, little self-supported WHs may exist [31]. The asymptotically flat spacetime is bonded with cylindrical WH solutions, which are noncompact [32]. Thus, the key question is whether compact objects such as asymptotically flat traversable WHs might exist within Einstein gravity without requiring the addition of phantom matter. Normal matter fields must violate the null energy requirements in this case [33,34]. The possibility that any EFE solution using ordinary matter fields may generate such WHs was unknown before the most recent study [35]. WH solutions in GR with two Dirac fields and an extra Maxwell field with the standard coupling between them were found in [35]. Two categories of WH solutions were represented: The first is an analytical solution describing a symmetric WH with respect to the throat sustained by massless and neutral fermions that are symmetric with respect to the throat. The symmetric arrangement of the matter fields and metric tensor is consistent with the other solution, which is normalizable and was found by numerical methods [36].

As observations attest, massive N-body simulations during recent decades successfully duplicated the formation of cosmic structures with increasing complexity and resolution [37–40]. One such recent review is presented in [41], which describes how a hydrodynamical model that predicts the evolution of cosmic structures up to the nonlinear regime is the culmination of complementary efforts to achieve a closed-form description. The nonlinear cosmic power spectrum may be expressed analytically and without parameters using a novel method founded on kinetic field theory; an overview of this technique can be found in [42]. According to all these methods, cosmic structures originate from the beginning seeds of overdensity in the power spectrum and travel forward through cosmic time to become cosmic structures. For the purpose of producing the nonlinear agglomerations that we witness in the real world, these methods need the initial phase-space configuration of overdensity seeds along with a dynamic description of their changes over cosmic time. Thus, based on the development of the phase-space volume of the original density seeds, they derive the statistical features of mass density perturbations of the whole observable universe. To date, though, these methods have failed to successfully infer the shape of individual mass density profiles of simulated or actual galaxies or galaxy clusters. The reason why one of these techniques has so far not succeeded in explaining the mass density profiles may be that there is no known physical correspondence between mass overdensity power spectrum variations and the finding of a given cosmic structure, like a (dark matter) halo.

The shape of the distribution of individual luminous matter, like the de-Vaucouleurs profile [43] or Jaffe profile [44], and many heuristic fitting functions have successfully been able to map out the forms of individual dark matter (DM) halos, like the Einasto profile [45] and the Navarro Frenk White profile [46,47]. Why the simulated and observed mass density distributions fit well with these formulae is still a mystery without a better grasp of how these profiles may be formed from more basic concepts. In this article, we are willing to determine the WH solutions by using different density profiles for the DM haloes along with the analysis of important factors associated with the WHs, including energy conditions, conservation equation, equation of state (EoS), complexity, and the active gravitational mass. Selecting an appropriate DM density model plays an important role in the formation of stable WH configurations. The Moore, Einasto, and Burkert profiles all have distinctive structural properties that play an important role in influencing the spacetime geometry. With its steep central cusp, Moore profile [48] represents a densely concentrated DM core, making it suitable

for studying strong gravitational effects close to the throat of the WH. In contrast, the Einasto profile, known for its smoother and flexible description of the DM halos over a larger radius range, has been utilised in recent wormholes studies as it can generate realistic distributions of energy-momentum in the modified theory of gravity [49]. Unlike cusped profiles, the Burkert profile [50] has cored structure that better fits galactic rotation curve data and reduces the dependence on exotic matter near the WH throat, making it an observationally viable framework for the WH configurations.

The work is set up as follows: Section 2 provides the EFE. The subsequent section provides a concise summary of the parametric mass density profiles for the most commonly used DM halo profiles of galaxies and clusters of galaxies. Section 3 describe the density profiles and involve the determination of the unknowns involved in the EFE. Section 3 discuses some factors that characterizes the WH solutions. Finally, the last section completes our analysis by providing some concluding remarks.

2 Basic formalism

In order to describe the geometry of the spacetime around the WH, we use the following spherically symmetric, time-independent line element

$$\begin{aligned} ds^2 &= g_{\gamma\mu}x^\gamma x^\mu \\ &= diag\left\{e^{2S}, -\left(1-\frac{\chi}{r}\right)^{-1}, -r^2, -r^2\sin^2\vartheta\right\}, \end{aligned} \tag{1}$$

where, $S = S(r)$ and $\chi = \chi(r)$ stands for redshift and shape function respectively. The famous EFE is given by the following mathematical expression

$$G_{\gamma\mu} = R_{\gamma\mu} - \frac{1}{2}Rg_{\gamma\mu} = \kappa T_{\gamma\mu}. \tag{2}$$

The anisotropic matter distribution as a relativistic source is given by the following mathematical expression

$$\begin{aligned} T_{\gamma\mu} &= (\rho + \mathcal{P}_{tan.})v_\gamma v_\mu - \mathcal{P}_{tan.}g_{\gamma\mu} \\ &\quad + (\mathcal{P}_{rad.} - \mathcal{P}_{tan.})x_\gamma x_\mu, \end{aligned} \tag{3}$$

where ρ, $\mathcal{P}_{tan.}$ and $\mathcal{P}_{rad.}$ stand for density, tangential and radial distribution of pressure, respectively. In addition, the radial unit four vector x_γ and the four-velocity vector v_γ fulfill the following relations: $x^\gamma x_\gamma = -1$ and $v^\gamma v_\gamma = 1$. After solving Eq. (2) and setting coupling constant $\kappa = 1$, we get the following expressions for the EFE

$$\rho = \frac{\chi'}{r^2}, \tag{4}$$

$$\mathcal{P}_{rad.} = \frac{1}{r^3}\left[-r\chi S' + r^2S' - \chi\right], \tag{5}$$

$$\begin{aligned} \mathcal{P}_{tan.} = \frac{1}{4r^3}\Big[&-2r^2\chi S'' + 2r^3S'' + r^2S'\chi' \\ &-r^2\chi S'^2 - r\chi S' + r^3S'^2 + 2r^2S' - 2r\chi' + 2\chi\Big]. \end{aligned} \tag{6}$$

The mathematical prediction of exotic matter (i.e., matter that defies the energy conditions), occurring inside WHs in GR [33], is ensured by analysing the null energy conditions (NEC). The expression for the NEC is given as

$$\rho + \mathcal{P}_{rad.} \geq 0 \ \ \& \ \ \rho + \mathcal{P}_{tan.} \geq 0.$$

After substitution following expressions for NEC result

$$\rho + \mathcal{P}_{rad.} = \frac{-r\chi S' + r^2S' - \chi}{r^3} + \frac{\chi'}{r^2}, \tag{7}$$

$$\rho + \mathcal{P}_{tan.} = \frac{r\left(2\left(r^2S'' + \chi'\right) + rS'\left(\chi' + 2\right) + r^2S'^2\right) - \chi\left(2r^2S'' + r^2S'^2 + rS' - 2\right)}{4r^3}. \tag{8}$$

Furthermore, Tables 4, 5, and 6 provide the complete description of the ECs, including NEC, weak EC, strong EC, and Dominant EC, along with their valid regions.

3 Different density models and the determination of the unknowns in EFE

In this section we attempt to find out the unknowns involved in the EFE by using three different DM density models. Each model uses a limited set of parameters with a physical interpretation to describe the mass density profile for the DM halos.

3.1 Model I: Einasto Profile

The Einasto density profile for the DM haloes is given by the following mathematical expression

$$\rho_E = \rho_0 \exp\left(-\frac{r}{h}\right)^{1/\alpha}, \tag{9}$$

where ρ_0, α, and h represent the central density, shape parameter (Einasto index), and scale length, respectively [51–54].

On comparing Eqs. (4) and (9), we obtain the following differential equation.

$$\frac{\chi'}{r^2} = \rho_0 \exp\left(-\frac{r}{h}\right)^{1/\alpha}. \tag{10}$$

After solving the above equation and using the throat condition (i.e., $\chi(r_0) = r_0$) following mathematical form of the function χ results

$$\chi = h^3\alpha\rho_0\Gamma\left(3\alpha, \left(\frac{r_0}{h}\right)^{1/\alpha}\right) - h^3\alpha\rho_0\Gamma\left(3\alpha, \left(\frac{r}{h}\right)^{1/\alpha}\right) + r_0, \tag{11}$$

The function χ is analysed graphically and found to meet all the requirements that are mandatory for the shape function to describe the WH geometry. Figure 1 provides the location of WH throat, which lies at $r_0 = 0.6$. Furthermore, Fig. 1 shows the asymptotic flatness and satisfaction of the flaring-out condition of the function χ. Table 1 illustrates the behaviour of the shape function at different points on the radial axis for some particular values of the parameters involved in the mathematical expressions corresponding to the shape function. The analysis of ECs is also conducted and depicted in Figs. 5 and 6. One can easily identify the validating region of ECs just by studying the Table 4. Consider zero tidal force, that is, $S = constant$, and substituting the values in Eqs. (4) and (5), following expressions for the matter variables is resulted

$$\mathcal{P}_{rad.} = \frac{1}{r^3}\left\{-r_0 - \alpha h^3\rho_0\left[\Gamma\left(3\alpha, \left(\frac{r_0}{h}\right)^{1/\alpha}\right) - \Gamma\left(3\alpha, \left(\frac{r}{h}\right)^{1/\alpha}\right)\right]\right\}, \tag{12}$$

$$\mathcal{P}_{tan.} = \frac{1}{4r^3}\left\{2\left(h^3\alpha\rho_0\left(\Gamma\left(3\alpha, \left(\frac{r_0}{h}\right)^{1/\alpha}\right) - \Gamma\left(3\alpha, \left(\frac{r}{h}\right)^{1/\alpha}\right)\right) + r_0\right) - 2r^3\rho_0\exp\left\{-\left(\frac{r}{h}\right)^{1/\alpha}\right\}\right\}. \tag{13}$$

3.2 Model II: Moore profile

The Moore profile for the DM halo is defined as follows [55,56]

$$\rho_M = \rho_0\left\{\frac{(r/\beta)^{-3/2}}{1-(r/\beta)^{3/2}}\right\}, \tag{14}$$

where β stands for scale radius. On comparing Eqs. (3) and (14), and solving the differential equation, we get the following expression for the shape function corresponding to Moore's profile

$$\begin{aligned}\chi|_M = &-\beta^3\rho_0\left(\frac{2}{3}\log\left(-\sqrt{\frac{r_0}{\beta}} + \frac{r_0}{\beta} + 1\right) + \frac{2}{3}\log\left(\sqrt{\frac{r_0}{\beta}} + 1\right)\right) \\ &+\beta^3\rho_0\left(\frac{2}{3}\log\left(\frac{r}{\beta} - \sqrt{\frac{r}{\beta}} + 1\right) + \frac{2}{3}\log\left(\sqrt{\frac{r}{\beta}} + 1\right)\right) + r_0,\end{aligned} \tag{15}$$

Graphical analysis of the function χ reveals that it satisfies every prerequisite needed for the shape function to describe the geometry of the WHs. According to Fig. 1, the WH throat is located at $r_0 = 0.6$. Furthermore, Fig. 1 shows the asymptotic flatness and satisfaction of the flaring-out condition of the function χ. Table 2 provides the values of the shape function versus radial distance r. In this case, the expressions for the matter variable attain the following form

$$\begin{aligned}\mathcal{P}_{rad.} = \frac{-1}{3r^3}\Bigg\{2\beta^3\rho_0\Bigg[&\log\left(\frac{r}{\beta} - \sqrt{\frac{r}{\beta}} + 1\right) + \log\left(\sqrt{\frac{r}{\beta}} + 1\right) - \log\left(-\sqrt{\frac{r_0}{\beta}} + \frac{r_0}{\beta} + 1\right) \\ &- \log\left(\sqrt{\frac{r_0}{\beta}} + 1\right)\Bigg] + 3r_0\Bigg\},\end{aligned} \tag{16}$$

$$\begin{aligned}\mathcal{P}_{tan.} = \frac{1}{2r^3}\Bigg\{\frac{1}{3}\beta^3\rho_0\Bigg[&-\frac{3r^2}{r^2 + \beta^2\sqrt{\frac{r}{\beta}}} + 2\log\left(\frac{r}{\beta} - \sqrt{\frac{r}{\beta}} + 1\right) + 2\log\left(\sqrt{\frac{r}{\beta}} + 1\right) \\ &- 2\log\left(-\sqrt{\frac{r_0}{\beta}} + \frac{r_0}{\beta} + 1\right) \\ &- 2\log\left(\sqrt{\frac{r_0}{\beta}} + 1\right)\Bigg] + r_0\Bigg\}.\end{aligned} \tag{17}$$

3.3 Model III: Berkert profile

The Berkert profile for the DM halo is given as [50,57]

$$\rho_B = \rho_0\left\{\frac{\left(\frac{r}{\beta} + 1\right)^{-1}}{\left(\frac{r}{\beta}\right)^2 + 1}\right\}. \tag{18}$$

The comparison of Eqs. (3) and (18) yield an ODE, and after solving this ODE following expression for the function χ results

$$\begin{aligned}\chi|_B = &-\beta^3\rho_0\left(\frac{1}{4}\log\left(\beta^2 + r_0^2\right) + \frac{1}{2}\log(\beta + r_0) - \frac{1}{2}\tan^{-1}\left(\frac{r_0}{\beta}\right)\right)\end{aligned}$$

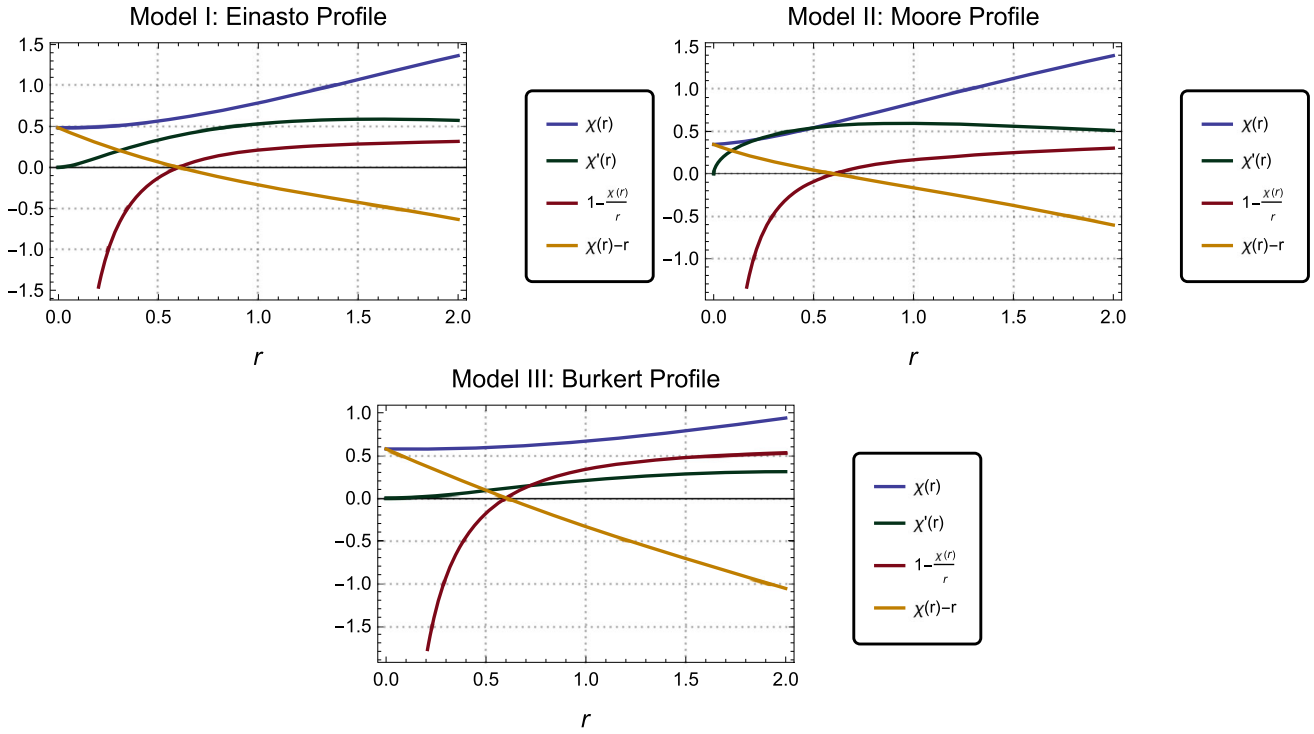

Fig. 1 Behavior of χ against radial distance r

Table 1 Analysis of shape function obtained from Einasto profile versus radial coordinate r for $h = 0.1$, $\alpha = 3$, $\rho_0 = 0.5$ and $r_0 = 0.6$

	r	χ	χ'	$1 - \frac{\chi}{r}$	$\chi - r$
1	0.0	0.483188	0.000001	− 4830.88	0.483188
2	0.2	0.493325	0.122204	− 1.46662	0.293325
3	0.4	0.533142	0.272108	− 0.332856	0.133142
4	0.6	0.6	0.390582	0	0
5	0.8	0.687116	0.141105	0.116	− 0.112884
6	1.0	0.788262	0.211738	0.072	− 0.211738

$$+\beta^3\rho_0\left(\frac{1}{4}\log\left(\beta^2+r^2\right)+\frac{1}{2}\log(\beta+r)-\frac{1}{2}\tan^{-1}\left(\frac{r}{\beta}\right)\right)+r_0. \tag{19}$$

The function χ is graphically analyzed and found to satisfy all the requirements for the shape function to characterize the geometry of the WHs. Figure 1 establishes that the WH throat is situated at $r_0 = 0.6$. Additionally, Fig. 1 demonstrates the function χ's asymptotic flatness and flaring out condition satisfaction. The behavior of the shape function at various radial axis locations is shown in Table 1 for certain values of the parameters used in the mathematical expressions that correspond to the shape function. The matter variable's expressions in this instance take on the following form

$$\mathcal{P}_{rad.}=\frac{1}{4r^3}\left\{\beta^3\rho_0\left[-\log\left(\beta^2+r^2\right)+\log\left(\beta^2+r_0^2\right)-2\log(\beta+r)+2\log(\beta+r_0)+2\tan^{-1}\left(\frac{r}{\beta}\right)-2\tan^{-1}\left(\frac{r_0}{\beta}\right)\right]-4r_0\right\}, \tag{20}$$

$$\mathcal{P}_{tan.}=\frac{1}{2r^3}\left\{\frac{1}{4}\beta^3\rho_0\left[\log\left(\beta^2+r^2\right)-\frac{4r^3}{(\beta+r)\left(\beta^2+r^2\right)}-\log\left(\beta^2+r_0^2\right)+2\log(\beta+r)-2\log(\beta+r_0)-2\tan^{-1}\left(\frac{r}{\beta}\right)+2\tan^{-1}\left(\frac{r_0}{\beta}\right)\right]+r_0\right\}. \tag{21}$$

4 Important factors associated with the wormholes

This section addresses the important factors associated with the WHs corresponding to the different DM halo density models.

Table 2 Analysis of shape function obtained from Moore profile versus radial coordinate r for $\beta = 1.5$, $\rho_0 = 0.5$ and $r_0 = 0.6$

	r	χ	χ'	$1-\frac{\chi}{r}$	$\chi - r$
1	0.0	0.346283	0.00001	− 34627.3	0.346273
2	0.2	0.399763	0.39172	− 0.998817	0.199763
3	0.4	0.491423	0.510631	− 0.228559	0.0914235
4	0.6	0.6	0.567855	-4.44089×10^{-16}	0
5	0.8	0.716338	0.591284	0.104578	− 0.0836621
6	1.0	0.835197	0.594794	0.164803	− 0.164803

4.1 Equation of state

The radial and tangential EoS corresponding to the Einasto profile are defined and given as follows

$$W_R\,|_E = \frac{\mathcal{P}_{rad.}}{\rho} = \frac{1}{r^3\rho_0}\left\{\exp\left[\left(\frac{r}{h}\right)^{1/\alpha}\right]\left(h^3\alpha\rho_0\left\{\Gamma\left(3\alpha,\left(\frac{r}{h}\right)^{1/\alpha}\right) - \Gamma\left(3\alpha,\left(\frac{r_0}{h}\right)^{1/\alpha}\right)\right\} - r_0\right)\right\}, \tag{22}$$

$$W_T\,|_E = \frac{\mathcal{P}_{tan.}}{\rho} = \frac{1}{2\rho_0 r^3}\left\{\exp\left[\left(\frac{r}{h}\right)^{1/\alpha}\right]\left(h^3\alpha\rho_0\left\{\Gamma\left(3\alpha,\left(\frac{r_0}{h}\right)^{1/\alpha}\right) - \Gamma\left(3\alpha,\left(\frac{r}{h}\right)^{1/\alpha}\right)\right\} + r_0\right) - r^3\rho_0\right\}. \tag{23}$$

For Moore's profile, EoS is given as

$$W_R\,|_M = \frac{1}{3\beta^2\rho r^2}\left\{\left(\sqrt{\frac{r}{\beta}}+1\right)\sqrt{\frac{r}{\beta}}\left[\beta\left(\sqrt{\frac{r}{\beta}}-1\right) - r\right]\left[2\beta^3\rho_0\left(\log\left(\frac{r}{\beta} - \sqrt{\frac{r}{\beta}}+1\right) + \log\left(\sqrt{\frac{r}{\beta}}+1\right) - \log\left(-\sqrt{\frac{r_0}{\beta}}+\frac{r_0}{\beta}+1\right) - \log\left(\sqrt{\frac{r_0}{\beta}}+1\right)\right) + 3r_0\right]\right\}, \tag{24}$$

$$W_T\,|_M = \frac{1}{-6r^2}\left\{-2\left(r^2+\beta^2\sqrt{\frac{r}{\beta}}\right)\log\left(\frac{r}{\beta} - \sqrt{\frac{r}{\beta}}+1\right) - 2\left(r^2+\beta^2\sqrt{\frac{r}{\beta}}\right)\log\left(\sqrt{\frac{r}{\beta}}+1\right) - \frac{3r_0\left(r^2+\beta^2\sqrt{\frac{r}{\beta}}\right)}{\beta^3\rho_0} + 2r^2\log\left(\sqrt{\frac{r_0}{\beta}}+1\right) + 3r^2 + 2\beta^2\sqrt{\frac{r}{\beta}}\log\left(-\sqrt{\frac{r_0}{\beta}} + 2r^2\log\left(-\sqrt{\frac{r_0}{\beta}}+\frac{r_0}{\beta}+1\right) + \frac{r_0}{\beta}+1\right) + 2\beta^2\sqrt{\frac{r}{\beta}}\log\left(\sqrt{\frac{r_0}{\beta}}+1\right)\right\}. \tag{25}$$

For the Burkert Profile, EoS attains the following form

$$W_R\,|_B = \frac{1}{4\beta^3\rho_0 r^3}(\beta+r)\left(\beta^2+r^2\right)\left\{\beta^3\rho_0\left(-\log\left(\beta^2+r^2\right) + \log\left(\beta^2+r_0^2\right) - 2\log(\beta+r) + 2\log(\beta+r_0) + 2\tan^{-1}\left(\frac{r}{\beta}\right) - 2\tan^{-1}\left(\frac{r_0}{\beta}\right)\right) - 4r_0\right\} \tag{26}$$

$$W_T\,|_B = -\frac{1}{8\beta^3\rho_0 r^3}(\beta+r)\left(\beta^2+r^2\right)\left\{\beta^3\rho_0\left(-\log\left(\beta^2+r^2\right) + \log\left(\beta^2+r_0^2\right) + 2\tan^{-1}\left(\frac{r}{\beta}\right) - 2\log(\beta+r) + 2\log(\beta+r_0) - 2\tan^{-1}\left(\frac{r_0}{\beta}\right)\right) - 4r_0\right\} - \frac{1}{2}. \tag{27}$$

We have analyzed W_R and W_T graphically and studied their behaviour. We found that these condition depicts opposite behaviour relative to one another.

4.2 Conservation equation

Using the general Tolman–Oppenheimer–Volkoff (TOV) equation, we examine the stability of the discovered WH solutions. The definition of the generalized TOV equation is [49]

$$-\frac{d\mathcal{P}_{rad.}}{dr} - \frac{S'}{2}(\rho + \mathcal{P}_{rad.}) - \frac{2}{r}(\mathcal{P}_{rad.} - \mathcal{P}_{tan.}) = 0. \tag{28}$$

A far more elegant method to describe the aforementioned TOV equation (28) is as the sum of the forces in an equilibrium.

$$F_A + F_H + F_G = 0, \tag{29}$$

where

$$F_A = -\frac{2}{r}(\mathcal{P}_{rad.} - \mathcal{P}_{tan.}), \quad F_H = -\frac{d\mathcal{P}_{rad.}}{dr} \quad and$$

$$F_G = -\frac{S'}{2}(\rho + \mathcal{P}_{rad.}). \tag{30}$$

Because we are considering zero tidal force i.e, $S = constant$, so $F_G = 0$ and our equilibrium scenario becomes

$$F_A + F_H = 0.$$

The expressions for hydrostatic and anisotropic forces corresponding to the Einasto profile is given as,

$$F_A\,|_E = \frac{1}{r^4}\left\{3r_0 + h^3\rho_0\left(3\alpha\Gamma\left(3\alpha, \left(\frac{r_0}{h}\right)^{1/\alpha}\right) - \exp\left\{-\left(\frac{r}{h}\right)^{1/\alpha}\right\}\left(\frac{r}{h}\right)^3 - 3\alpha\Gamma\left(3\alpha, \left(\frac{r}{h}\right)^{1/\alpha}\right)\right)\right\}, \tag{31}$$

$$F_H\,|_E = -\frac{1}{r^4}\left\{3r_0 + h^3\rho_0\left(3\alpha\Gamma\left(3\alpha, \left(\frac{r_0}{h}\right)^{1/\alpha}\right) - \exp\left\{-\left(\frac{r}{h}\right)^{1/\alpha}\right\}\left(\frac{r}{h}\right)^3 - 3\alpha\Gamma\left(3\alpha, \left(\frac{r}{h}\right)^{1/\alpha}\right)\right)\right\}. \tag{32}$$

For Moore's profile

$$\begin{aligned} F_A\,|_M = &-\frac{1}{3r^4}\left\{-\frac{9r_0}{\mathcal{K}} + 6\beta^3\mathcal{P}_0\left(\log\left(-\sqrt{\frac{r_0}{\beta}} + \frac{r_0}{\beta} + 1\right) + \log\left(\sqrt{\frac{r_0}{\beta}} + 1\right)\right) + \frac{\beta^3\mathcal{P}_0 r}{\beta\sqrt{\frac{r}{\beta}} + r}\right. \\ &+ \frac{\beta^3\mathcal{P}_0\left(2r - \beta\sqrt{\frac{r}{\beta}}\right)}{\beta - \beta\sqrt{\frac{r}{\beta}} + r} \\ &- 6\beta^3\mathcal{P}_0\left(\log\left(\frac{r}{\beta} - \sqrt{\frac{r}{\beta}} + 1\right) + \log\left(\sqrt{\frac{r}{\beta}} + 1\right)\right)\Bigg\}, \end{aligned} \tag{33}$$

$$\begin{aligned} F_H\,|_M = &\frac{1}{3r^4}\left\{-\frac{9r_0}{\mathcal{K}} + 6\beta^3\mathcal{P}_0\left(\log\left(-\sqrt{\frac{r_0}{\beta}} + \frac{r_0}{\beta} + 1\right) + \log\left(\sqrt{\frac{r_0}{\beta}} + 1\right)\right) + \frac{\beta^3\mathcal{P}_0 r}{\beta\sqrt{\frac{r}{\beta}} + r}\right. \\ &+ \frac{\beta^3\mathcal{P}_0\left(2r - \beta\sqrt{\frac{r}{\beta}}\right)}{\beta - \beta\sqrt{\frac{r}{\beta}} + r} \\ &- 6\beta^3\mathcal{P}_0\left(\log\left(\frac{r}{\beta} - \sqrt{\frac{r}{\beta}} + 1\right) + \log\left(\sqrt{\frac{r}{\beta}} + 1\right)\right)\Bigg\} \end{aligned} \tag{34}$$

For Burkert profile

$$\begin{aligned} F_A\,|_B = &-\frac{1}{r^4}\left\{\frac{1}{4}\beta^3\rho_0\left(-3\log\left(\beta^2 + r^2\right) + \frac{4r^3}{(\beta + r)\left(\beta^2 + r^2\right)} + 3\log\left(\beta^2 + r_0^2\right)\right.\right. \\ &-6\log(\beta + r) + 6\log(\beta + r_0) \\ &\left.\left.+6\tan^{-1}\left(\frac{r}{\beta}\right) - 6\tan^{-1}\left(\frac{r_0}{\beta}\right)\right) - 3r_0\right\}, \end{aligned} \tag{35}$$

$$\begin{aligned} F_H\,|_B = &\frac{1}{r^4}\left\{\frac{1}{4}\beta^3\rho_0\left(-3\log\left(\beta^2 + r^2\right) + \frac{4r^3}{(\beta + r)\left(\beta^2 + r^2\right)}\right.\right. \\ &+3\log\left(\beta^2 + r_0^2\right) - 6\log(\beta + r) + 6\log(\beta + r_0) \\ &\left.\left.+6\tan^{-1}\left(\frac{r}{\beta}\right) - 6\tan^{-1}\left(\frac{r_0}{\beta}\right)\right) - 3r_0\right\}. \end{aligned} \tag{36}$$

The graphical analysis of the equilibrium scenario reveals that these forces cancel each other completely and ensure the satisfaction of the conservation equation and hence, the stability of the WH solutions.

4.3 Complexity

Herrera [58] presented a new concept of complexity within self-gravitating fluids having static spherically symmetric geometry in GR [58]. He performed an orthogonal decomposition of the curvature tensor to get a peculiar mathematical entity symbolized as Y_{TF}. This was named as the complexity factor, having the following formula

$$Y_{TF} = (\mathcal{P}_{rad.} - \mathcal{P}_{tan.}) - \frac{1}{2r^3}\int_{r_0}^{r} x^3\rho'(x).dx. \tag{37}$$

This concept was widely used to study various astrophysical applications by Herrera et al. [59–62] and other researchers [5,63–71]. With the constraint $Y_{TF} = 0$, one can analyze a homogeneous fluid under isotropic pressure with less complexity in the population. This concept helps to study and classify less-complex WHS supported with exotic matter wormholes. This concept could lead to tracking the dynamical evolution of minimal complex WHs, despite being supported by irregular and anisotropic matter [72,73]. After substituting the values following expressions for the complexity factor associated with the WHs for different density profiles is

$$Y_{TF}\,|_E = \frac{h^3\rho_0}{2r^3}\left\{\Gamma\left(3\alpha + 1, \left(\frac{r_0}{h}\right)^{1/\alpha}\right) - 3\alpha\Gamma\left(3\alpha, \left(\frac{r_0}{h}\right)^{1/\alpha}\right) + \exp\left\{-\left(\frac{r}{h}\right)^{1/\alpha}\right\}\left(\frac{r}{h}\right)^3 - \Gamma\left(3\alpha + 1, \left(\frac{r}{h}\right)^{1/\alpha}\right) + 3\alpha\Gamma\left(3\alpha, \left(\frac{r}{h}\right)^{1/\alpha}\right)\right\} - \frac{3r_0}{2r^3}. \tag{38}$$

$$Y_{TF}\,|_M = \frac{r_0\left(\frac{r}{\beta}\right)^{3/2}\left(r^3\sqrt{\frac{r}{\beta}}+2\beta r^2+\beta^3\sqrt{\frac{r}{\beta}}\right)\left(\beta^3\rho_0\sqrt{\frac{r_0}{\beta}}-3\beta\left(\left(\frac{r_0}{\beta}\right)^{3/2}+1\right)\right)}{2r^5\left(\sqrt{\frac{r}{\beta}}+1\right)\left(\beta+r\sqrt{\frac{r}{\beta}}\right)\left(\beta-\beta\sqrt{\frac{r}{\beta}}+r\right)\left(\left(\frac{r_0}{\beta}\right)^{3/2}+1\right)}. \tag{39}$$

$$Y_{TF}\,|_B = -\frac{r_0\left(3\beta^3+r_0^2\left(3\beta-\beta^3\rho_0\right)+3\beta^2 r_0+3r_0^3\right)}{2r^3\left(\beta+r_0\right)\left(\beta^2+r_0^2\right)}. \tag{40}$$

We observed that the complexity factor of the WHs corresponding given density models increases steadily with time. The complexity factor rises as the contribution of parameters α and β grows. Therefore, it is probable that the density models will support increasingly intricate systems. However, it is found that the complexity plays a part in the structure of WH and that its contribution steadily diminishes after reaching a particular radial coordinate value, such as $r = 2$. This is illustrated graphically in Fig. 7.

4.4 Active Mass Function

The strength of the gravitational flux of the astrophysical object, in our case, a WH is measured by the active gravitational mass. Within the range between the throat r_0 and an outside radial distance r, the WH's active mass is

$$M = 4\pi\int_{r_0}^{r}\rho(x)x^2\,dx. \tag{41}$$

After substituting the values and solving the above integral, the following expressions of the mass function for different density models result

$$M\,|_E = 4\pi h^3\alpha\rho_0\left\{\Gamma\left(3\alpha,\left(\frac{r_0}{h}\right)^{1/\alpha}\right)-\Gamma\left(3\alpha,\left(\frac{r}{h}\right)^{1/\alpha}\right)\right\}. \tag{42}$$

$$\begin{aligned}M\,|_M = \frac{8}{3}\pi\beta^3\rho_0\Bigg\{&-\log\left(-\sqrt{\frac{r_\circ}{\beta}}+\frac{r_\circ}{\beta}+1\right)\\&-\log\left(\sqrt{\frac{r_\circ}{\beta}}+1\right)+\log\left(\frac{r}{\beta}-\sqrt{\frac{r}{\beta}}+1\right)\\&+\log\left(\sqrt{\frac{r}{\beta}}+1\right)\Bigg\}.\end{aligned} \tag{43}$$

$$\begin{aligned}M\,|_B = \pi\beta^3\rho_0\Big\{&\log\left(\beta^2+r^2\right)-\log\left(\beta^2+r_0^2\right)\\&+2\log(\beta+r)-2\log\left(\beta+r_0\right)\\&-2\tan^{-1}\left(\frac{r}{\beta}\right)+2\tan^{-1}\left(\frac{r_0}{\beta}\right)\Big\}.\end{aligned} \tag{44}$$

5 Final remarks

Scientists have been significantly fascinated by the scientific research of WH geometry over the past decades. As a result, WHs in the galactic halo zone were proposed by the URC and NFW DM density profiles. In this article, we researched the WH geometry under the influence of the Einasto, Moore, and Burkert DM galactic halo profiles. The main conclusions of the present study are discussed in detail below:

The DM halo profiles (including Einasto, Moore, and Burkert profiles) were among the first topics we covered. By comparing the energy density of GR with the energy density of DM halo profiles, we were able to determine the shape functions corresponding to these profiles. We have analyzed derived features such as the condition of flare-out of the generated shape function against an asymptotic background. It is noteworthy that the parameters of the model involved play an important role in the manner in which the WHs are analyzed. We saw that the requirement of flare-out is met near the throat. Furthermore, Tables 1, 2, and 3, and Fig. 1 provides the comparison between the shape functions obtained from each density profile. The behavior of the shape function χ corresponding to different DM density profiles has been systematically analyzed through both graphical and tabular data (Fig. 1 and Tables 1, 2 and 3). As evident from Fig. 1, all three models satisfy the fundamental geometric constraint, ensuring the validity of the flare-out condition near the throat of the WH. The Einasto profile exhibits a constant rise in χ, which indicates the existence of stable WH geometry. The Moore profile exhibits a more concentrated central structure, and in line with its cuspy density character, χ' displays a stronger gradient close to the throat. The Burkert profile, on the other hand, has a soft core, resulting in a less steep $\chi(r)$ growth and less central curvature. The data in the table, which compares the growth behavior and derivative character of $\chi(r)$ among models, quantitatively supports these findings. This demonstrates that the geometrical structure and feasibility of WH configurations are significantly influenced by the density profile that is chosen.

After that, we talked about ECs for every density model with the right free parameter selections. Figures 2, 3, and 4 displays the plot of energy density vs radial distance, indicating positively decreasing behavior over spacetime. Additionally, the behavior of $\rho+\mathcal{P}$ denotes the violation of radial NEC. According to fixed values of parameters $\alpha = 3, h = 0.1, \rho_0 = 0.5, \beta = 1.5$ and $r_0 = 0.6$, it was

Table 3 Analysis of shape function obtained from Burkert profile versus radial coordinate r for $\beta = 1.5$, $\rho_0 = 0.5$ and $r_0 = 0.6$

	r	χ	χ'	$1-\frac{\chi}{r}$	$\chi - r$
1	0.0	0.574539	0	− 57452.9	0.574529
2	0.2	0.575739	0.0173388	− 1.8787	0.375739
3	0.4	0.58309	0.0589648	− 0.457726	0.18309
4	0.6	0.6	0.110837	0	0
5	0.8	0.6274	0.162479	0.21575	− 0.1726
6	1.0	0.664555	0.207692	0.335445	− 0.335445

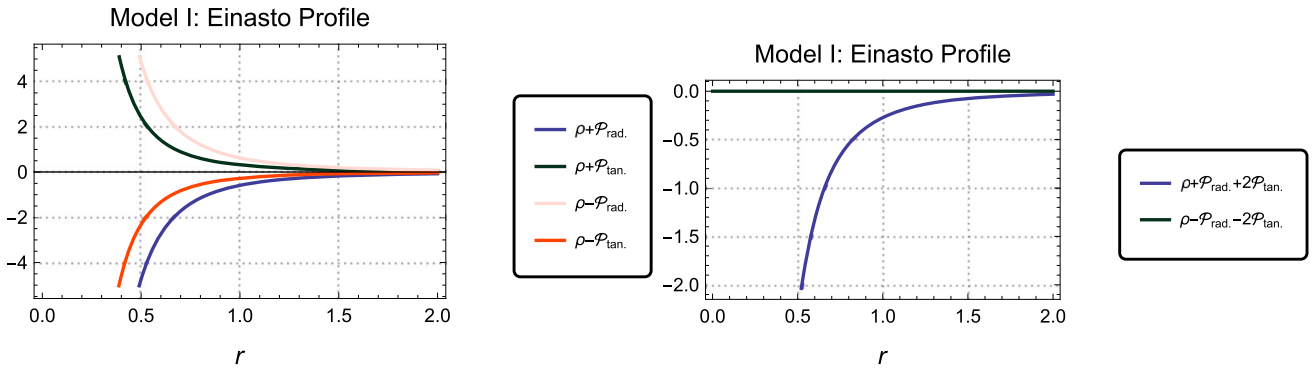

Fig. 2 Analysis of ECs corresponding to Einasto profile

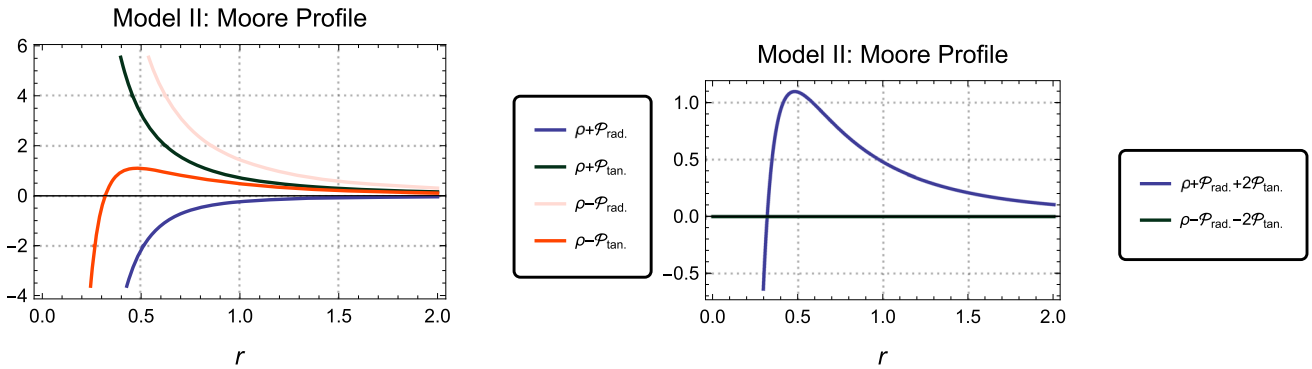

Fig. 3 Analysis of ECs

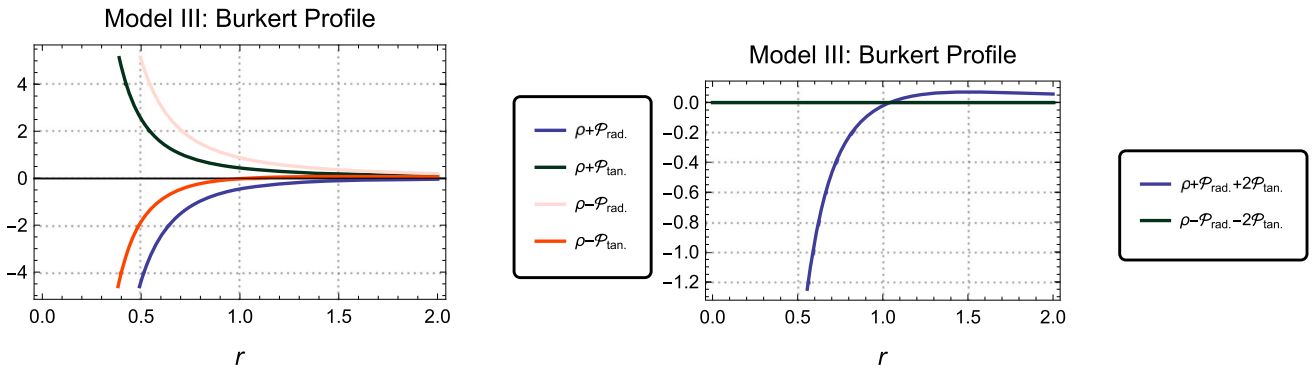

Fig. 4 Analysis of ECs

Table 4 Values of the ECs resulted from Einasto profile against the radial coordinate r for $h = 0.1$, $\alpha = 3$, $\rho_0 = 0.5$ and $r_0 = 0.6$

	r	$\rho + \mathcal{P}_{rad.}$	$\rho + \mathcal{P}_{tan.}$	$\rho - \mathcal{P}_{rad.}$	$\rho - \mathcal{P}_{tan.}$	$\rho + \mathcal{P}_{rad.} + 2\mathcal{P}_{tan.}$	$\rho - \mathcal{P}_{rad.} - 2\mathcal{P}_{tan.}$
1	0.0	-5.95352×10^{47}	2.97676×10^{50}	5.95352×10^{50}	-2.97676×10^{50}	0	0
2	0.2	− 74.3479	37.2955	74.591	− 37.0524	0	0.243117
3	0.4	− 9.26577	4.70055	9.4011	− 4.56522	1.77636×10^{-15}	0.135335
4	0.6	− 2.73461	1.41047	2.82095	− 1.32414	4.44089×10^{-16}	0.0863376
5	0.8	− 1.14909	0.604099	1.2082	− 0.544993	2.22045×10^{-16}	0.0591057
6	1.0	− 0.586326	0.314328	0.628655	− 0.271998	0	0.0423292

Table 5 Values of the ECs resulted from Moore profile against the radial coordinate r for $\beta = 1.5$, $\rho_0 = 0.5$ and $r_0 = 0.6$

	r	$\rho + \mathcal{P}_{rad.}$	$\rho + \mathcal{P}_{tan.}$	$\rho - \mathcal{P}_{rad.}$	$\rho - \mathcal{P}_{tan.}$	$\rho + \mathcal{P}_{rad.} + 2\mathcal{P}_{tan.}$	$\rho - \mathcal{P}_{rad.} - 2\mathcal{P}_{tan.}$
1	0.0	-3.46283×10^{38}	1.73141×10^{38}	3.46283×10^{38}	-1.73141×10^{38}	0	5.80948×10^{19}
2	0.2	− 40.1774	29.8817	59.7634	− 10.2957	0	19.586
3	0.4	− 4.48705	5.43497	10.8699	0.947916	0	6.38288
4	0.6	− 1.2004	2.17758	4.35515	0.977174	0	3.15475
5	0.8	− 0.475217	1.16149	2.32298	0.686273	0	1.84776
6	1.0	− 0.240404	0.714996	1.42999	0.474592	0	1.18959

Table 6 Values of the ECs resulted from Moore profile against the radial coordinate r for $\beta = 1.5$, $\rho_0 = 0.5$ and $r_0 = 0.6$

	r	$\rho + \mathcal{P}_{rad.}$	$\rho + \mathcal{P}_{tan.}$	$\rho - \mathcal{P}_{rad.}$	$\rho - \mathcal{P}_{tan.}$	$\rho + \mathcal{P}_{rad.} + 2\mathcal{P}_{tan.}$	$\rho - \mathcal{P}_{rad.} - 2\mathcal{P}_{tan.}$
1	0.0	-5.74539×10^{50}	2.8727×10^{50}	5.74539×10^{50}	-2.8727×10^{50}	0	1.0
2	0.2	− 71.5339	36.2004	72.4009	− 35.3335	0	0.866941
3	0.4	− 8.74225	4.73966	9.47932	− 4.0026	0	0.73706
4	0.6	− 2.4699	1.54283	3.08566	− 0.927066	0	0.615764
5	0.8	− 0.971517	0.739632	1.47926	− 0.231884	0	0.507748
6	1.0	− 0.456863	0.436124	0.872247	− 0.020739	0	0.415385

shown that NEC is violated at the throat. Tables 4, 5, and 6 provide the complete description of the ECs, including NEC, weak EC, strong EC and Dominant EC along with their valid regions. The radial and tangential EoS are calculated and analysed graphically in Fig. 5 for the density models under consideration. From Fig. 5 it is observed that the radial EoS shows increasing behaviour near the WH throat while an opposite pattern can be observed in the tangential EoS case.

The comparative analysis of ECs and EoS parameters (as depicted in Figs. 2, 3, 4 and 5 and Tables 4, 5 and 6) provides distinct characteristics of the Einasto, Moore, and Burkert profiles in supporting stable WH structures. Breaching of NEC is observed near the WH throat for all three models, which ensures the need of exotic matter for sustaining the WH geometry. NEC violation decreases as r increases, showing that the exotic matter is localized. The core structure of the Burkert profile shows milder and more localized violations, while the Moore and Einasto profiles causes sharper NEC violations. The radial and tangential EoS parameters exhibit different trends for different density profiles. Whereas the Einasto and Moore profiles exhibit sudden changes in W_R and W_T close to the throat that stabilize only asymptotically, the Burkert profile has smooth, well-defined transitions of both parameters across the domain. This leads to a physically more reasonable method of approaching constant values at large radii. These findings demonstrate that the Burkert profile provides more physically realistic WH solutions with reduced exotic matter requirements, while the steeper gradients of the Moore and Einasto profiles make them particularly valuable for studying WHs in strong-field gravitational scenarios.

Furthermore, we have analysed important factors associated with the WHs including, equilibrium analysis, active mass function, and complexity of the WHs solutions. The conservation analysis involves the study of the behaviour of the hydrostatic and anisotropic forces. The TOV equation provides mathematical proof that these forces will balance each other out in the long run. Consequently, it is reasonable to say that the WH solutions for all the models under study found in this research are classically stable. These forces are

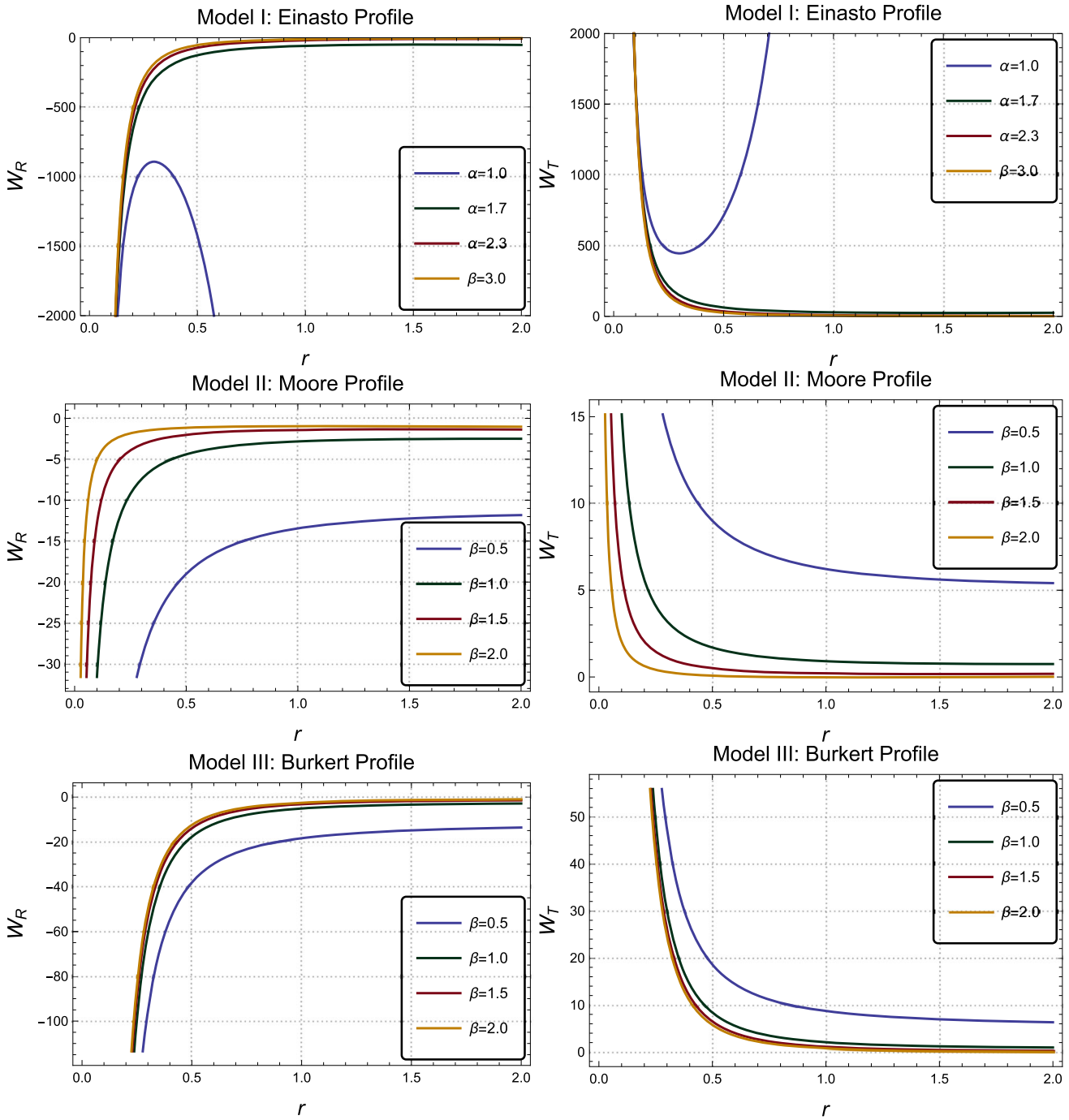

Fig. 5 Analysis of EoS

graphically demonstrated in Fig. 6 for each density model. Readers who are interested in learning more about this issue can consult [74], where the writers have thoroughly examined it. Moreover, the active gravitational mass is calculated and analysed graphically in Fig. 8 for each density model. The active gravitational mass M shows a monotonic radial increase in all profiles, and the results assure physical consistency. The Moore profile has the most rapid rate of mass accumulation because of its very sharp central cusp, and the Einasto profile has the slowest rate of increase because of its large core. The Burkert profile is intermediate, having moderate compactness as well as improved physical plausibility. These systematic differences show how the inner slope of density determines both the efficiency of mass generation and the resulting spacetime geometry.

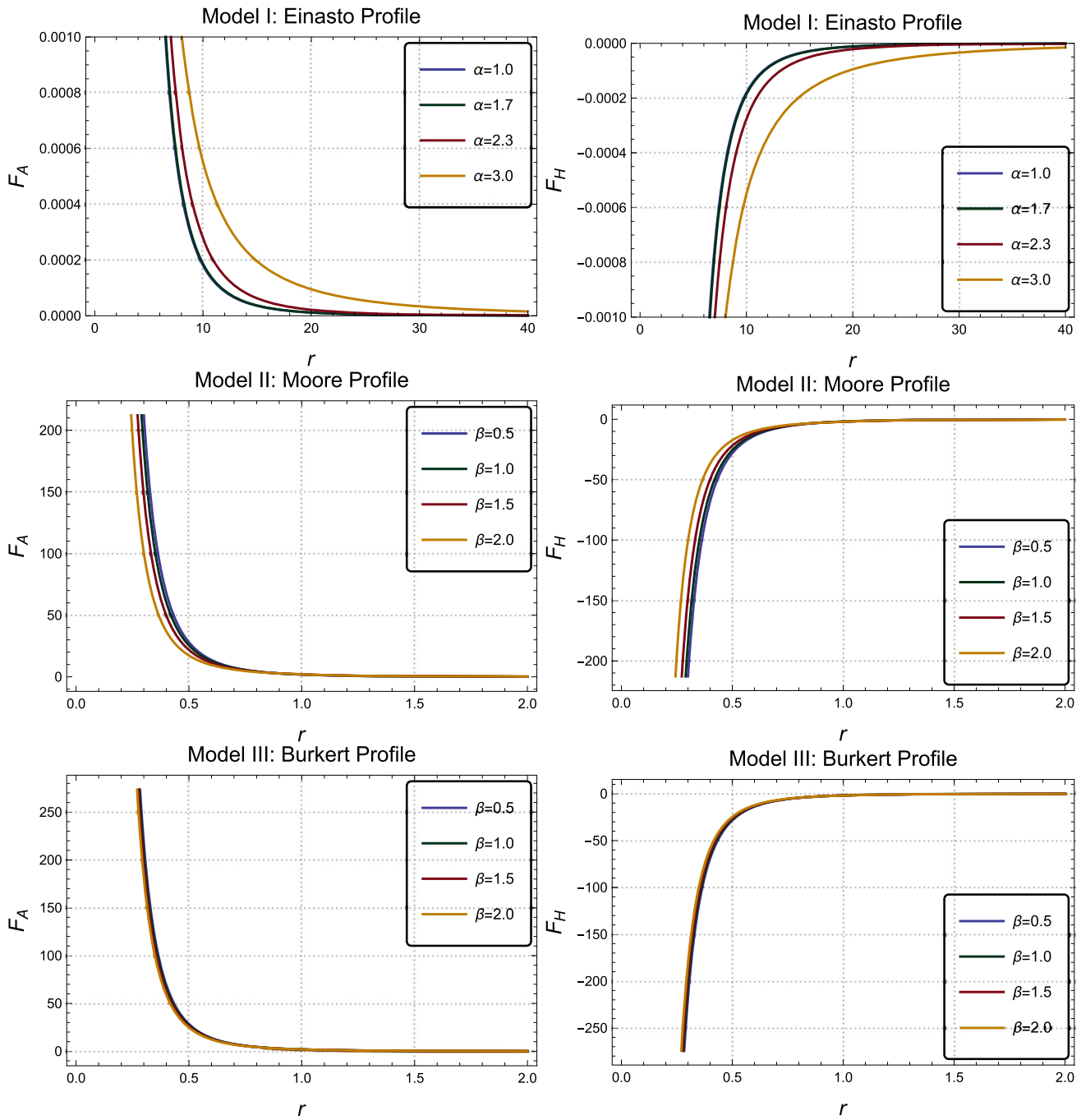

Fig. 6 Analysis of conservative forces

Motivated by Herrera's work [58], we have taken into account the irrotational, time-independent spacetime metric of the WH and subsequently analyzed the complexity factor. The complexity factor Y_{TF} has a negative and monotonic increasing behavior for all three models from large negative values close to the WH throat and slowly converging to zero. The Burkert profile is found to have the largest initial negative value, with the most significant anisotropic effects close to the core, followed by the Moore and Einasto profiles. All profiles, however, display smooth convergence, which indicates stable configurations. This action supports the view that complexity decreases with radial distance, increasing the physical viability of the WH structures. The key finding from our research is that, in GR, realistic geometries of DM WHs may be found in the natural environment around different galaxy haloes.

It is important to note that the Einasto, Burkert, and Moore profiles analyzed in this research are not just theoretical mod-

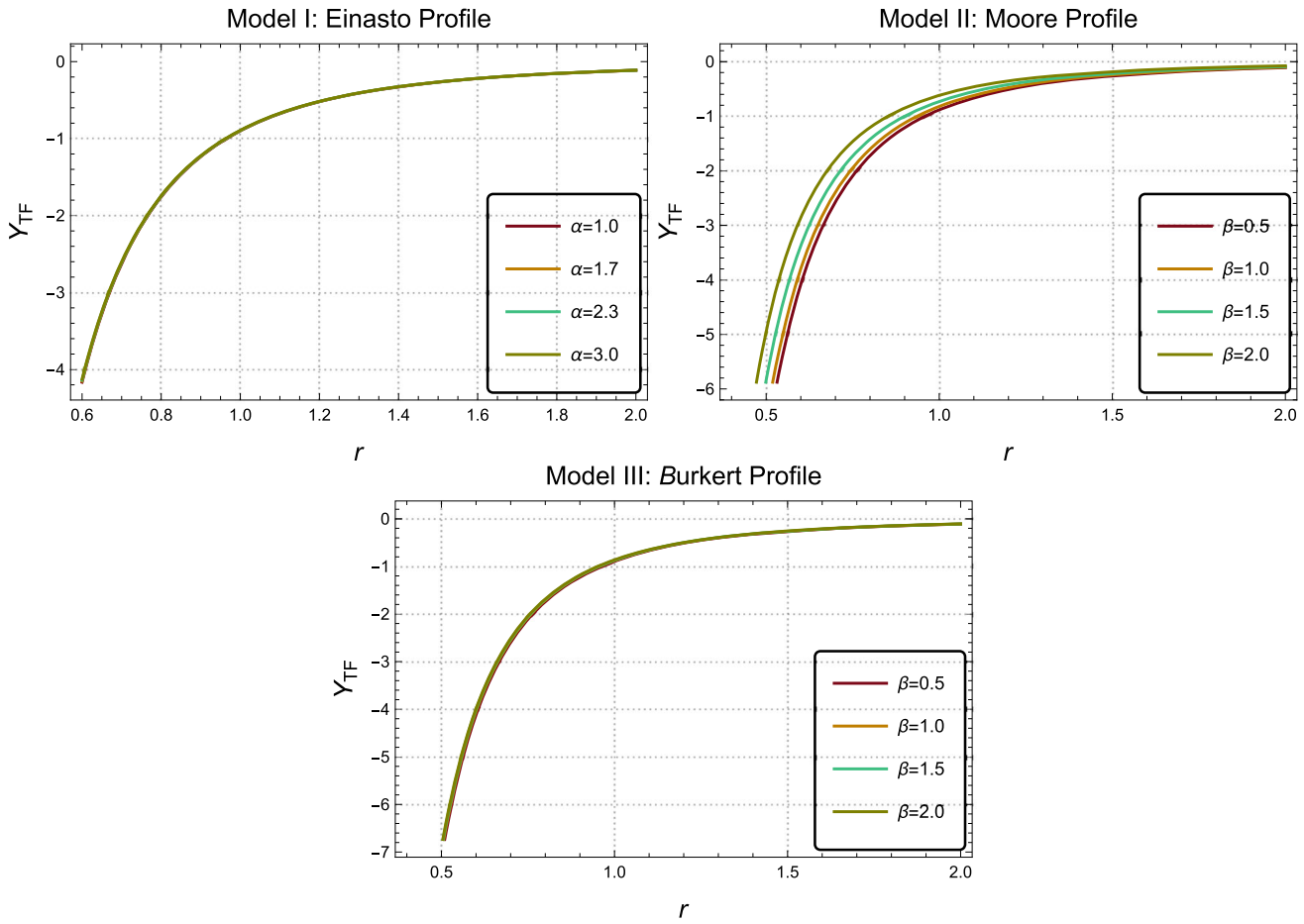

Fig. 7 Complexity of the system

els, but have also been well implemented to describe several observed systems. For example, the Einasto profile has been found to yield very good fits to the Milky Way and other spiral galaxies' mass distribution [75,76]. The Burkert profile is typically employed to explain the cored density profiles of dwarf spheroidal galaxies and low-surface-brightness galaxies [50,77,78], while the cuspy Moore profile has been used in the modeling of galaxy clusters and high-resolution simulations [48,79]. Outside galactic dynamics, the same dark matter distributions have also been explored around compact objects, such as black holes [80,81], neutron stars [82], and gravastars [83]. These observational links reinforce the physical applicability of the wormhole solutions obtained here and make one suppose that such geometries may, in principle, be tested within reasonable astrophysical situations.

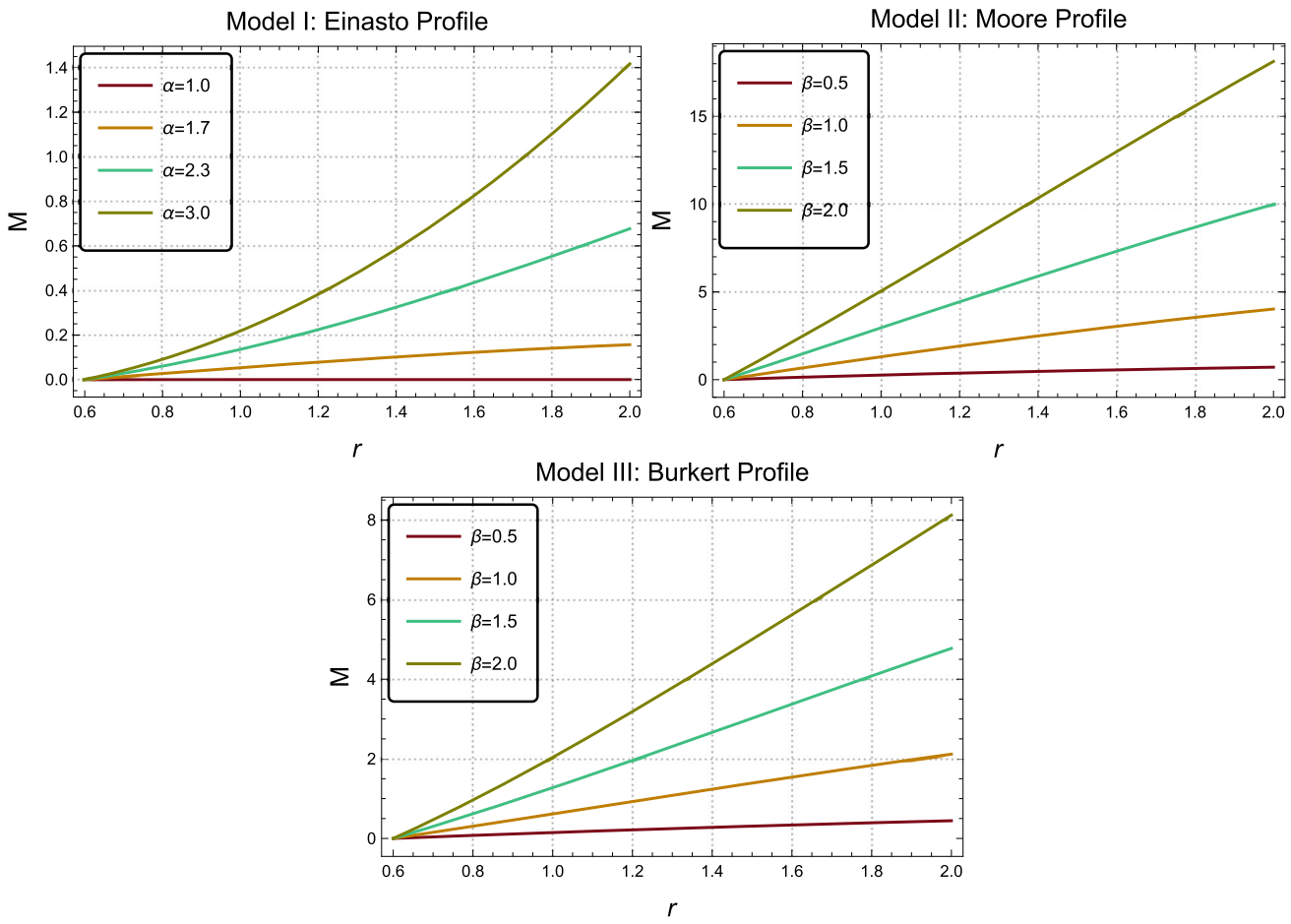

Fig. 8 Mass function

Author contributions ZY, MR, OAA: Writing [Pleaseinsertintopreamble] review & editing, Supervision, Conceptualization, Writing [Pleaseinsertintopreamble] original draft, Visualization, Validation, Software, Methodology, Investigation. OAA, MMA, MA, ZY: Validation, Methodology, Formal analysis. Software, Methodology, Investigation.

Funding The present work did not receive any funding.

Data Availibility This manuscript has no associated data or the data will not be deposited. [Author's Comment: Data sharing not applicable to this article as no datasets were generated or analysed during the current study.]

Code availability My manuscript has no associated code/software. [Author's comment: Code/Software sharing not applicable to this article as no code/software was generated or analysed during the current study.].

Declarations

Conflict of interest The authors have no Conflict of interest with respect to the publication of the present paper.

Funded by SCOAP[3].

References

1. A. Einstein, Phys. Today **35**, 45 (1982)
2. G. Holton, Am. J. Phy. **28**, 627 (1960)
3. A. Einstein, in The meaning of relativity (Springer, 1922), p. 54
4. A. Einstein, W. Perrett, G. Jeffery, Ann. Phys. **354**, 769 (1916)
5. Z. Yousaf, A. Adeel, M. Rizwan, G. Mustafa, A. Ali, Int. J. Geom. Methods Mod. Phys., 2550093 (2025)
6. Z. Yousaf, B. Almutairi, M. Rizwan, T. Ganesan, M. Bhatti, Int. J. Mod. Phys. D **34**, 2450072 (2025)
7. A. Einstein, N. Rosen, Phys. Rev. **48**, 73 (1935)
8. C.W. Misner, J.A. Wheeler, Ann. Phys. **2**, 525 (1957)

9. M.S. Morris, K.S. Thorne, Am. J. Phys. **56**, 395 (1988)
10. I.H. Redmount, Prog. Theor. Exp. Phys. **73**, 1401 (1985)
11. T. Damour, S.N. Solodukhin, Phys. Rev. D **76**, 024016 (2007)
12. J.H. Simonetti, M.J. Kavic, D. Minic, D. Stojkovic, D.-C. Dai, Phys. Rev. D **104**, L081502 (2021)
13. D.-C. Dai, D. Minic, D. Stojkovic, Phys. Rev. D **98**, 124026 (2018)
14. D.-C. Dai, D. Stojkovic, Phys. Rev. D **100**, 083513 (2019)
15. V. De Falco, E. Battista, S. Capozziello, M. De Laurentis, Eur. Phys. J. C **81**, 157 (2021)
16. E. Battista, S. Capozziello, A. Errehymy, Eur. Phys. J. C **84**, 1314 (2024)
17. M.Y. Khlopov, B. Malomed, Y.B. Zeldovich, Mon. Not. R. Astron. Soc. **215**, 575 (1985)
18. D.-C. Dai, D. Minic, D. Stojkovic, Eur. Phys. J. C **80**, 1 (2020)
19. V. De Falco, M. De Laurentis, S. Capozziello, Phys. Rev. D **104**, 024053 (2021)
20. V. De Falco, Phys. Rev. D **108**, 024051 (2023)
21. J. Maldacena, A. Milekhin, Phys. Rev. D **103**, 066007 (2021)
22. P.L. McFadden, N. Turok, Phys. Rev. D **71**, 086004 (2005)
23. K.A. Bronnikov, R.A. Konoplya, Phys. Rev. D **101**, 064004 (2020)
24. K. Bronnikov, V. Melnikov, H. Dehnen, Phys. Rev. D **68**, 024025 (2003)
25. K. Bronnikov, S.-W. Kim, Phys. Rev. D **67**, 064027 (2003)
26. P. Kanti, B. Kleihaus, J. Kunz, Phys. Rev. D **85**, 044007 (2012)
27. V. De Falco, E. Battista, S. Capozziello, M. De Laurentis, Phys. Rev. D **101**, 104037 (2020)
28. J. Gonzalez, F. Guzman, O. Sarbach, Class. Quant. Grav. **26**, 015010 (2008)
29. M.A. Cuyubamba, R.A. Konoplya, A. Zhidenko, Phys. Rev. D **98**, 044040 (2018)
30. E. Di Grezia, E. Battista, M. Manfredonia, G. Miele, Eur. Phys. J. Plus **132**, 537 (2017)
31. T. Harko, F.S. Lobo, M. Mak, S.V. Sushkov, Phys. Rev. D **87**, 067504 (2013)
32. K. Bronnikov, V. Krechet, Phys. Rev. D **99**, 084051 (2019)
33. M.S. Morris, K.S. Thorne, Am. J. Phys. **56**, 395 (1988)
34. S. Bolokhov, K. Bronnikov, S. Krasnikov, M. Skvortsova, Grav. Cosmol. **27**, 401 (2021)
35. J.L. Blázquez-Salcedo, C. Knoll, E. Radu, Phys. Rev. Lett. **126**, 101102 (2021)
36. V. De Falco, E. Battista, S. Capozziello, M. De Laurentis, Phys. Rev. D **103**, 044007 (2021)
37. A. Del Popolo, M. Le Delliou, Galaxies **5**, 17 (2017)
38. J.S. Bullock, M. Boylan-Kolchin, Ann. Rev. Astron. Astrophys. **55**, 343 (2017)
39. M. Kuhlen, M. Vogelsberger, R. Angulo, Phys. Dark Universe **1**, 50 (2012)
40. C.S. Frenk, S.D. White, Ann. Phys. **524**, 507 (2012)
41. B.M. Schäfer, in Formation of the First Black Holes (World Scientific, 2019), pp. 23–44
42. M. Bartelmann, E. Kozlikin, R. Lilow, C. Littek, F. Fabis, I. Kostyuk, C. Viermann, L. Heisenberg, S. Konrad, D. Geiss, Ann. Phys. **531**, 1800446 (2019)
43. G. de Vaucouleurs, Ann. d'Astrophys. **11**, 247 (1948)
44. W. Jaffe, Mon. Not. R. Astron. Soc. **202**, 995 (1983)
45. J. Einasto, Trudy Astrofizich. Inst. Alma-Ata **5**, 87 (1965)
46. J.F. Navarro, in Symposium-international astronomical union (Cambridge University Press, 1996), vol. 171, p. 255
47. J.F. Navarro, C.S. Frenk, S.D. White, arXiv preprint arXiv:astro-ph/9508025 (1995)
48. B. Moore, S. Ghigna, F. Governato, G. Lake, T. Quinn, J. Stadel, P. Tozzi, Astrophys. J. **524**, L19 (1999)
49. Z. Yousaf, K. Bamba, B. Almutairi, M. Bhatti, M. Rizwan, Nucl. Phys. B **1018**, 116997 (2025)
50. A. Burkert, Astrophys. J. **447**, L25 (1995)
51. J. Einasto, Astron. Nachr. **291**, 97 (1969)
52. E. Retana-Montenegro, E. Van Hese, G. Gentile, M. Baes, F. Frutos-Alfaro, Astron. Astrophys. **540**, A70 (2012)
53. M. Baes, Astron. Astrophys. **667**, A47 (2022)
54. P.F. de Salas, K. Malhan, K. Freese, K. Hattori, M. Valluri, J. Cosmol. Astropart. Phys. **2019**, 037 (2019)
55. B. Moore, F. Governato, T. Quinn, J. Stadel, G. Lake, Astrophy. J. **499**, L5 (1998)
56. B. Moore, Nature **370**, 629 (1994)
57. A. Burkert, Astrophys. J. Lett **447**, L25 (1995)
58. L. Herrera, Phys. Rev. D. **97**, 044010 (2018)
59. L. Herrera, A. Di Prisco, J. Ospino, Phys. Rev. D **98**, 104059 (2018)
60. L. Herrera, A. Di Prisco, J. Ospino, Phys. Rev. D **99**, 044049 (2019)
61. L. Herrera, A. Di Prisco, J. Carot, Phys. Rev. D **99**, 124028 (2019)
62. L. Herrera, Phys. Rev. D **101**, 104024 (2020)
63. S. Bhattacharya, S. Nalui, J. Math. Phys. **64**, (2023)
64. Z. Yousaf, K. Bamba, M.Z. Bhatti, U. Farwa, Int. J. Geom. Methods Mod. Phys. **21**, 2430005 (2024)
65. G. Panotopoulos, A. Rincon, I. Lopes, Phys. Lett. B **856**, 138901 (2024)
66. M.Z. Bhatti, M.Y. Khlopov et al., Int. J. Geom. Methods Mod. Phys. 2540014 (2025a)
67. Z. Yousaf, H. Asad et al., Int. J. Geom. Methods Mod. Phys. 2550145 (2025d)
68. N. Iqbal, S. Khan, M. Alshammari, W.W. Mohammed, M. Ilyas, Eur. Phys. J. C **85**, 372 (2025)
69. H.M.A. Mahmoud, S. Khan, L.M. Abdalgadir, Phys. Dark Universe **49**, 101974 (2025)
70. S. Khan, J. Rayimbaev, I. Ibragimov, S. Muminov, A. Dauletov, A. Abdujabbarov, Phys. Scr. **100**, 085302 (2025)
71. M.Z. Bhatti, B. Almutairi et al., Int. J. Geom. Methods Mod. Phys. **22**, 2550001 (2025)
72. A. Malik, T. Naz et al., Int. J. Geom. Methods Mod. Phys. **21**, 2450186 (2024)
73. A. Malik, T. Naz et al., Int. J. Geom. Methods Mod. Phys. **21**, 2440003 (2024)
74. O. Sokoliuk, A. Baransky, Eur. Phys. J. C **81**, 1 (2021)
75. J.F. Navarro, E. Hayashi, C. Power, A. Jenkins, C.S. Frenk, S.D. White, V. Springel, J. Stadel, T.R. Quinn, Mon. Not. R. Astron. Soc. **349**, 1039 (2004)
76. D. Merritt, J.F. Navarro, A. Ludlow, A. Jenkins, Astrophys. J. **624**, L85 (2005)
77. P. Salucci, A. Burkert, Astrophys. J. **537**, L9 (2000)
78. W. De Blok, S.S. McGaugh, V.C. Rubin, Astron. J. **122**, 2396 (2001)
79. T. Fukushige, J. Makino, Astrophys. J. **557**, 533 (2001)
80. O.Y. Gnedin, J.R. Primack, Phys. Rev. Lett. **93**, 061302 (2004)
81. M.Z. Bhatti, Phys. Dark Universe **49**, 101953 (2025)
82. M. Razeira, A. Mesquita, C.A. Vasconcellos, R.O. Gomes, Int. J. Mod. Phys. E **20**, 109 (2011)
83. D. Horvat, S. Ilijić, A. Marunović, Class. Quantum Grav. **28**, 195008 (2011)